


Article

In Silico and In Vitro Analyses of Multiple Terpenes Predict Cryptotanshinone as a Potent Inhibitor of the Omicron Variant of SARS-CoV-2

Asmita Shrestha ¹, Siddha Raj Upadhyaya ¹, Bimal K. Raut ¹, Salyan Bhattarai ², Khaga Raj Sharma ¹, Niranjana Parajuli ^{1,3,*}, Jae Kyung Sohng ^{3,*} and Bishnu P. Regmi ^{4,*}

¹ Central Department of Chemistry, Tribhuvan University, Kirtipur, Kathmandu 44618, Nepal; sanzillshrestha@gmail.com (A.S.); upadhyayasiddharaj@gmail.com (S.R.U.); rautbimal777@gmail.com (B.K.R.); khaga.sharma@cdc.tu.edu.np (K.R.S.)

² Paraza Pharma, Inc., 2525 Avenue Marie-Curie, Montreal, QC H4S 2E1, Canada; salyanbiotech@gmail.com

³ Institute of Biomolecule Reconstruction (iBR), Department of Life Science and Biochemical Engineering, Sun Moon University, Asan 31460, Republic of Korea

⁴ Department of Chemistry, Florida Agricultural and Mechanical University, Tallahassee, FL 32307, USA

* Correspondence: authors: niranjan.parajuli@cdc.tu.edu.np (N.P.); sohng@sunmoon.ac.kr (J.K.S.); bishnu.regmi@famou.edu (B.P.R.)

Abstract: The severe acute respiratory syndrome coronavirus 2 (SARS-CoV-2) Omicron variant (B.1.1.529) underwent a substantial number of alterations, and the accompanying structural mutations in the spike protein prompted questions about the virus's propensity to evade the antibody neutralization produced by prior infection or vaccination. New mutations in SARS-CoV-2 have raised serious concerns regarding the effectiveness of drugs and vaccines against the virus; thus, identifying and developing potent antiviral medications is crucial to combat viral infections. In the present study, we conducted a detailed in silico investigation that involves molecular docking, density functional (DFT) analysis, molecular dynamics (MD) simulations, and pharmacological analysis followed by an in vitro study with the spike protein. Among fifty terpenes screened, cryptotanshinone and saikosaponin B2 were found to be potent S1-RBD spike protein inhibitors, displaying considerable hydrogen bond interactions with key binding site residues, significant binding affinity, and high reactivity attributed to band gap energy. In addition, 100 ns molecular dynamics (MD) simulations further substantiated these findings, showcasing the stability of the compounds within a biological environment. With favorable pharmacokinetic properties and a low half inhibitory concentration (IC₅₀) of 86.06 ± 1.56 μM, cryptotanshinone inhibited S1-RBD of the SARS-CoV-2 Omicron variant. Our findings account for in-depth research on cryptotanshinone as a SARS-CoV-2 inhibitor.

Keywords: spike protein; COVID-19; Omicron variant; terpenes



Citation: Shrestha, A.; Upadhyaya, S.R.; Raut, B.K.; Bhattarai, S.; Sharma, K.R.; Parajuli, N.; Sohng, J.K.; Regmi, B.P. In Silico and In Vitro Analyses of Multiple Terpenes Predict Cryptotanshinone as a Potent Inhibitor of the Omicron Variant of SARS-CoV-2. *Processes* **2024**, *12*, 230. <https://doi.org/10.3390/pr12010230>

Academic Editor: Giancarlo Cravotto

Received: 15 December 2023

Revised: 15 January 2024

Accepted: 19 January 2024

Published: 21 January 2024



Copyright: © 2024 by the authors. Licensee MDPI, Basel, Switzerland. This article is an open access article distributed under the terms and conditions of the Creative Commons Attribution (CC BY) license (<https://creativecommons.org/licenses/by/4.0/>).

1. Introduction

Even if the COVID-19 global pandemic has officially ended after three years, acute illness screening and management do not appear to be the end of the struggle against COVID-19. There is a probable concern that the present vaccinations may not be sufficiently effective against newly emerging strains of SARS-CoV-2 variants, and a considerable proportion of people with weak immune systems may not acquire complete protection following vaccination [1]. Thus, advancing the discovery of simple oral coronavirus medications is imperative [2].

The further mutation of the Omicron variant, coupled with its high transmissibility and infectivity, increased risk of reinfection, and potential impediments to immunotherapies, have raised concerns about therapeutic efficacy [3,4]; thus, any breakthrough toward the development of potent antiviral medications is essential. The spike protein is primarily

responsible for virus pathogenesis and organ tropism in SARS-CoV-2 [5], and the Omicron variant exhibits a distinctive profile with 37 mutations in the spike protein, notably 15 within the receptor-binding domain (RBD) [6]. Omicron's spike, specifically S1-RBD, demonstrates a significant affinity for angiotensin-converting enzyme 2 (ACE-2), surpassing that of other prototypes [7,8]. Therefore, antiviral medicines that specifically target the spike protein are important for the cure of SARS-CoV-2 infections. The antiviral potential of natural products (NPs) against numerous viruses including SARS-CoV-2 has been effective [9]. NPs possess structural diversity that exceeds that of synthetic chemicals and can employ mechanisms of action via routes distinct from those of conventional treatments. NPs, such as alkaloids, flavonoids, and terpenes have demonstrated antiviral effects by strengthening the immune system and inhibiting viral entrance and replication [10,11]. Terpenes, naturally occurring isoprene-based small molecules found in a variety of medicinal plants, exhibit chemical diversity with a multitude of medicinal actions [12], including the ability to possess anti-malarial [13], anti-bacterial [14], anti-cancer [15,16], anti-neurological disorder [17], anti-viral [18], anti-inflammatory [19], and anti-oxidant activity [20], anti-cardiovascular disease effects [21,22], and antiviral properties against SARS-CoV [23] and Human Immunodeficiency Virus 1 [24]. Consequently, the use of terpenes as prototypes for developing effective pharmacotherapeutic agents might be an effective strategy. Regarding SARS-CoV infections, terpenes reportedly impede the binding of the S1-RBD of SARS-CoV-2 to the ACE-2 receptor, thereby limiting the virus's capacity to enter host cells [25]. Considering the therapeutic potential of terpenes, we used computational methods to study additional natural terpenes targeting S1-RBD of the SARS-CoV-2 Omicron variant followed by an in vitro study.

Computational methodologies employing algorithm-based virtual screening methods for rapidly evaluating enormous libraries of pharmaceuticals and natural compounds are the most practical ways to gain insights into new phytoconstituents to develop antiviral medications against SARS-CoV-2 [26]. This study includes the molecular docking of 50 terpenes with the S1-RBD of the Omicron variant. To assess the level of reactivity in each protein's binding pocket, DFT analysis based on the E_{LUMO} , E_{HOMO} , and band gap energy of these terpenes was conducted, and the stability behavior of the identified potential drug candidates with the target protein was confirmed by MD simulations. Considering the MD simulation results and pharmacological properties, an in vitro assay of a potent drug candidate was carried out. Thereby, the focus of this study is to assess effective medications that inhibit the spike protein of SARS-CoV-2 using comprehensive in silico techniques and further validation acquired through in vitro investigation.

2. Materials and Methods

2.1. Preparation of Ligand Database

The terpenes were selected considering their antiviral activities reported earlier (Table S1) and were retrieved utilizing the PubChem (<https://pubchem.ncbi.nlm.nih.gov/>) [27] and ChemSpider (<http://www.chemspider.com/>) [28] web servers in the .sdf format. Subsequently, PyMOL software version 4.3 (<https://pymol.org/>) [29] was used to convert them into the .pdb format. The structures of some terpenes are shown in Figure 1. Utilizing the AutoDock tool, the ligands were prepared for molecular docking purposes in the .pdbqt format. The chemical structure of the selected 50 terpenes is displayed in Figure S1.

2.2. Preparation of Protein

Initially, the alterations in the S1-RBD spike protein of the Omicron variant were identified from the literature [30]. The S1-RBD crystal structure (PDB ID: 7QNW) was then acquired from the RCSB PDB webserver (<https://www.rcsb.org/>), and each amino acid was examined individually, i.e., 15 mutations in S1-RBD were analyzed, confirmed, and cleaned via removal of the water molecules, heteroatoms, and undesirable chains. Subsequently, the AutoDock tool (version 1.5.6, Scripps Research Institute, La Jolla, CA,

USA) was used to prepare the protein by adding Kollmann charges and polar hydrogen atoms and was finally saved into the .pdbqt format (<https://vina.scripps.edu/>) [31].

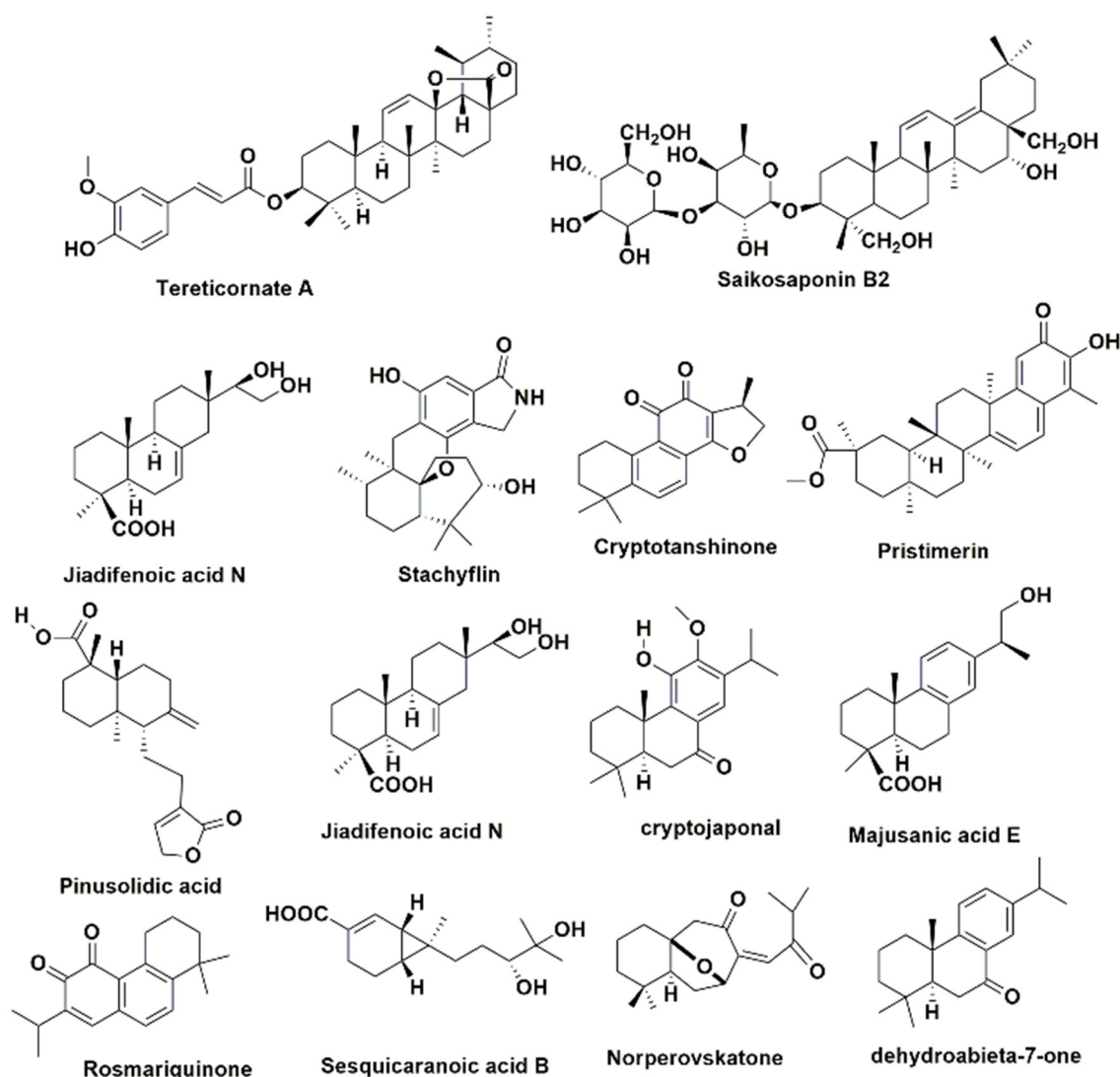


Figure 1. Structures of some of the naturally occurring terpenes used in the computational study.

2.3. Molecular Docking

The AutoDock tool was utilized to execute the molecular docking of all the selected terpenes within a $60 \times 60 \times 60 \text{ \AA}$ grid box's dimensions, created and centered on the key residues responsible for S1-RBD interaction. The key interacting amino acid residues of S1-RBD that are responsible for binding with ACE-2 [32,33] were chosen as a binding pocket of S1-RBD for the docking purpose. Using BIOVIA Discovery Studio Visualizer 2020, each generated 9 poses were analyzed. Based on the significant binding energy and substantial hydrogen bond interactions in addition to the hydrophobic interactions with key residues of S1-RBD, the compounds were screened. To reduce the possibility of false-positive results, the docking protocol was verified by re-docking and superimposition methods ($\text{RMSD} \leq 2 \text{ \AA}$), which guaranteed the correctness and consistency of the docking results [34,35]

2.4. DFT Analysis

A DFT analysis was used to examine the reactivity and efficacy of saikosaponin B2, cryptotanshinone, and luteolin (reference ligand) against the S1-RBD of the Omicron variant. The 3-parameter Becke, Lee–Yang–Parr (B3LYP) correlation function was employed

to acquire the energies of the highest occupied molecular orbital (HOMO) and lowest unoccupied molecular orbital (LUMO) [36]. The following equation estimates the band energy gap (ΔE_{gap}):

$$\Delta E_{\text{gap}} = E_{\text{LUMO}} - E_{\text{HOMO}} \quad (1)$$

The ionization potential (IP) and electron affinity (EA) of the molecules were calculated using the given equations [37]:

$$\text{IP} = -E_{\text{HOMO}} \quad (2)$$

$$\text{EA} = -E_{\text{LUMO}} \quad (3)$$

The following equations were used to determine the global softness (S), global hardness (η), chemical potential (μ), and electronegativity (χ) [38]:

$$S = 1/\eta \quad (4)$$

$$\eta = \Delta E/2 \quad (5)$$

$$\chi = (I + A)/2 \approx -\mu \quad (6)$$

$$\omega = \mu^2/2\eta \quad (7)$$

2.5. MD Simulation

The MD simulations for examining the stability of anticipated protein–ligand complexes were executed using GROMACS 5.1.1, and the GROMOS 43a1 force field was chosen [39]. The ligand topology parameters were generated using PRODRG [40]. For solvation, a cubic box model (10 Å side length margin) was employed with the SPC water model [41]. Utilizing the steepest energy minimization, the existing network of solvent molecules, ions, and protein–ligand complexes was relaxed over 50,000 steps. To support the initial phase of equilibrium by maintaining the constant particle number, volume, and temperature (NVT), the subsequent steps involved using the Berendsen temperature coupling technique. The Parrinello–Rahman barostat was then utilized to conduct the final equilibrium phase, ensuring that the constant particle number, pressure, and temperature (NPT) were maintained throughout the procedure. Ultimately, at 300 K, a production run was performed for 100 ns. A comparative analysis was conducted utilizing the root mean square deviation (RMSD), root mean square fluctuation (RMSF), the radius of gyration (R_g), solvent accessible surface area (SASA), and H-bondings. The plots were created using ORIGINPRO® 2023 and analyzed through the Xmgrace application.

2.6. Pharmacokinetics Study

The drug-resembling features of cryptotanshinone and luteolin were identified using the SwissADME web tool (<http://www.swissadme.ch/>) [42]. Additionally, the pkCSM (<http://structure.bioc.cam.ac.uk/pkcsm>) and ProTox II servers (<https://tox-new.charite.de/>) [43,44] were used for absorption, distribution, metabolism, excretion, and toxicity (ADMET) studies and toxicity class prediction.

2.7. In Vitro S1-RBD Assay

The in vitro S1-RBD assay was conducted following the procedure outlined in the literature [45] with slight modifications. Initially, varying concentrations of 100 μL cryptotanshinone were loaded onto a 96-well plate coated plate with S1-RBD of SARS-CoV-2 Omicron variant (ACROBiosystems, Newark, DE, USA; Catalog No. RP-13), followed by preincubation at 37 °C for 4 h. After three washes with a PBS buffer (pH 7.2), the plate was blocked with a blocking solution (1% BSA and 0.05% Tween-20 in PBS) and again incubated for 1 h. After three washes, 100 μL of hACE2 receptor protein (Novatein Biosciences Inc., Woburn, MA, USA; Catalog no.: PR-nCoV-4) (0.1–0.2 $\mu\text{g}/\text{mL}$) and binding buffer (0.1% BSA in PBS, pH 7.2) were added and again incubated for 1 h. After three more washes, to each well of the plate, goat anti-human IgG-Fc, HRP (Novatein Biosciences, Woburn, MA, USA;

Catalog no.: NB-A0101) (100 μ L of 1:5000) was added and subjected to incubation at 37 °C for 30 min. Finally, the reaction of 3,3',5,5'-tetramethylbenzidine (TMB) was stopped by adding a stop solution, and the absorption was measured at 450 nm. The following formula was employed to evaluate the inhibitory activity:

$$\text{Percent inhibition} = \left(\frac{A_{\text{control}} - A_{\text{sample}}}{A_{\text{control}}} \right) \times 100,$$

where A_{control} = absorbance of the control; A_{sample} = absorbance of the sample.

3. Results and Discussion

3.1. Molecular Docking Analysis

With regard to the molecular docking, redocking strategies were utilized to ensure its accuracy and robustness. The protocol was validated with an RMSD of 0.621 Å, which is less than 2 Å, for the reference structure of luteolin [46]. Figure S2 illustrates the superimposition of the reference structure. Following the docking protocol validation, 50 terpenes chosen for their antiviral properties were docked using AutoDock tools with S1-RBD of the Omicron variant. The binding energies for the docked compounds are shown in Table S2. Based on the interactions with key amino acid residues of S1-RBD, particularly Lys 440 [47], which plays an important role in immune evasion and establishing a strong binding with ACE-2 through hydrogen bonds, and considering the binding scores, the docking results revealed saikosaponin B2 and cryptotanshinone as effective inhibitors of the target protein. Figures 2–4 represent the 2D and 3D interaction of cryptotanshinone, saikosaponin B2, and the reference compound luteolin, respectively, with the target protein.

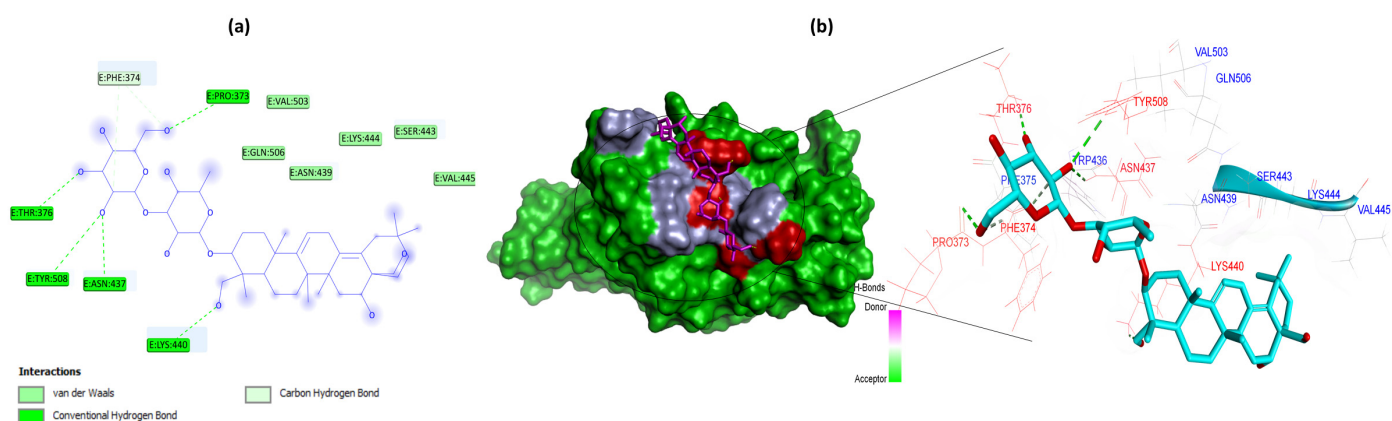


Figure 2. (a) 2D representation of saikosaponin B2-S1-RBD complex and (b) surface view showing binding pocket for ligand; red color shows polar bond region (hydrogen bond), and blue color shows non-polar bond region (hydrophobic interactions); the inset on the right shows a 3D structure with different interactions.

Hydroxyl groups of the oxane ring of saikosaponin B2 were found to show hydrogen bonds with Phe 374, Thr 376, Asn 437, and Tyr 508. In addition, the oxane ring's hydroxymethyl group showed an H-bond with Pro 373, Phe 374, and Lys 440 of the S1-RBD with a -9.3 kcal/mol binding energy. Cryptotanshinone forms pi-pi T-shaped interactions with Phe 374 and Phe 375 and pi-alkyl interaction with Trp 436 of S1-RBD. According to a previous study by Ong et al., Trp 436 could have contributed to the inactivation of human coronaviruses after absorption of UVC light by Trp 436 [48]. The keto group of cyclohexadienedione of cryptotanshinone forms hydrogen bond interaction with the amine group of Lys 440 with -7.6 kcal/mol binding energy. Lys 440 is one of the S1-RBD amino acid residues involved in immune escape [49] and is responsible for establishing an effective interaction between ACE-2 and S1-RBD of the Omicron variant [47]. It is noteworthy that saikosaponin B2 and cryptotanshinone exhibit an H bond with Lys 440. Luteolin with

significant S1-RBD interactions exhibited -7.1 kcal/mol binding energy. These compounds' binding energies and hydrogen bonds in addition to other interactions with the S1-RBD are displayed in Table 1. Moreover, by using these kinds of computational approaches and theoretical strategies for molecular docking, it is feasible to create an explanatory hypothesis regarding the mode of action of metabolites.

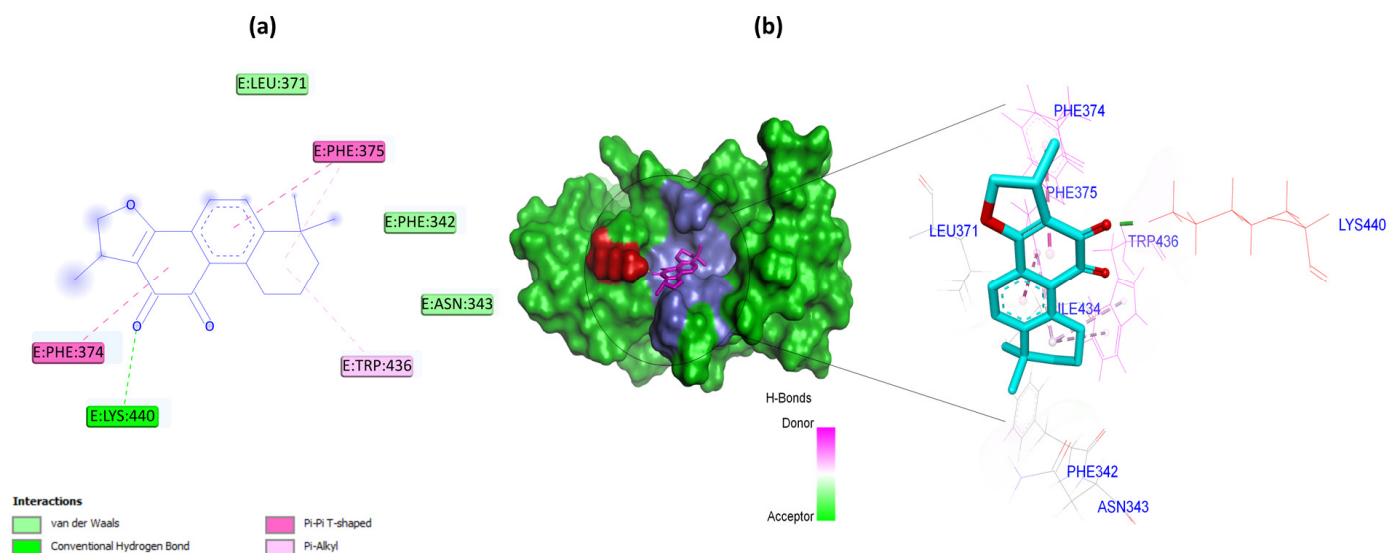


Figure 3. (a) 2D representation of cryptotanshinone-S1-RBD complex and (b) surface view showing binding pocket for ligand; red color shows polar bond region (hydrogen bond), and blue color shows non-polar bond region (hydrophobic interactions); the inset on the right shows a 3D structure with different interactions.

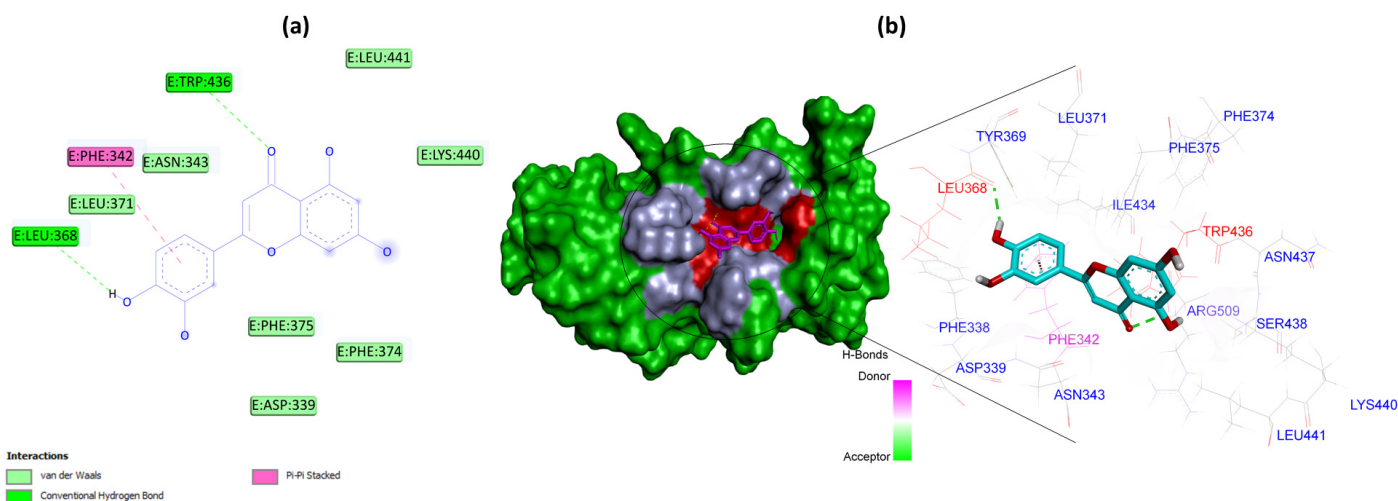


Figure 4. (a) 2D representation of luteolin-S1-RBD complex and (b) surface view showing binding pocket for ligand; red color shows polar bond region (hydrogen bond), and blue color shows non-polar bond region (hydrophobic interactions); the inset on the right shows a 3D structure with different interactions.

Table 1. Binding affinity and the interacting amino acid residues of the S1-RBD spike protein of the SARS CoV-2 Omicron variant with potent terpenes including reference ligand.

Ligands	PubChem ID	Binding Affinity (kcal/mol)	Amino Acid Residues with Different Interactions
Saikosaponin B2	21637642	−9.3	Hydrogen bond: Pro 373, Phe 374, Thr 376, Asn 437, Lys 440, Tyr 508 Van der Waals: Val 503, Gln 506, Asn 439, Lys 444, Ser 443, Val 445
Cryptotanshinone	160254	−7.6	Hydrogen bond: Lys 440 Pi-Pi T-shaped: Phe 374, Phe 375 Pi-Alkyl: Trp 436 Van der Waals: Phe 342, Asn 343
Luteolin	5280445	−7.1	Hydrogen bond: Trp 436, Leu 368 Pi-Pi Stacked: Phe 342 Van der Waals: Asp 339, Phe 374, Phe 375

3.2. DFT Analysis-Based Band Gap Results

The HOMO, LUMO, and band energy gap ($E_{LUMO} - E_{HOMO}$) are regarded as crucial quantum parameters since they are used to determine how a molecule interacts with other species either through protein–ligand interactions or ligand–ligand interactions [50]. Molecules having a low band energy gap are typically more polarizable and possess strong chemical reactivity and low kinetic stability [51]. Pearson’s principle of maximum hardness states that the compound with the lowest chemical hardness exhibits maximum reactivity [52]. Similarly, electronegativity indicates the electrophilic nature of compounds; the higher the electronegativity, the greater the chemical reactivity with the target protein [53]. In addition, a compound with a higher value of both chemical potential and electrophilicity index acts as a good electrophile rather than a nucleophile [54], indicating more reactivity with catalytic protein.

In the current study, cryptotanshinone, saikosaponin B2, and luteolin (reference compound) were selected for DFT analysis. The results show that cryptotanshinone has a low band gap of HOMO and LUMO, i.e., 0.11842 kcal/mol compared to the reference compound ($\Delta E_{gap} = 0.14692$ kcal/mol), representing its effective reactivity and binding affinity as demonstrated in Figure 5. However, saikosaponin B2 is comparatively less reactive than the reference compound due to a high band gap energy ($\Delta E_{gap} = 0.18415$ kcal/mol). Moreover, the global hardness, softness, electrophilic nature, chemical potential, and electrophilicity index that are measures of the reactivity (Table 2), indicate the strong potency of cryptotanshinone toward the respective SARS-CoV-2 protein.

Table 2. DFT results in terms of the chemical reactivity descriptors.

Ligands	E_{LUMO} (kcal/mol)	E_{HOMO} (kcal/mol)	Band Gap Energy (ΔE_{gap}) (kcal/mol)	Ionization Potential (I) (kcal/mol)	Electron Affinity (A) (kcal/mol)	Global Hardness (η) (kcal/mol)	Global Softness (S) (kcal/mol)	electronegativity (χ) (kcal/mol)	Chemical Potential (μ) (kcal/mol)	Electrophilicity Index (ω) (kcal/mol)
Saikosaponin B2	−0.01839	−0.20254	0.18415	0.20254	0.01839	0.092075	10.8607	0.110465	−0.110465	0.06626
Cryptotanshinone	−0.10747	−0.22589	0.11842	0.22589	0.10747	0.05921	16.8890	0.16668	−0.16668	0.23461
Luteolin	−0.007595	−0.22287	0.14692	0.22287	0.07595	0.7346	13.61285	0.14941	−0.14941	0.011162

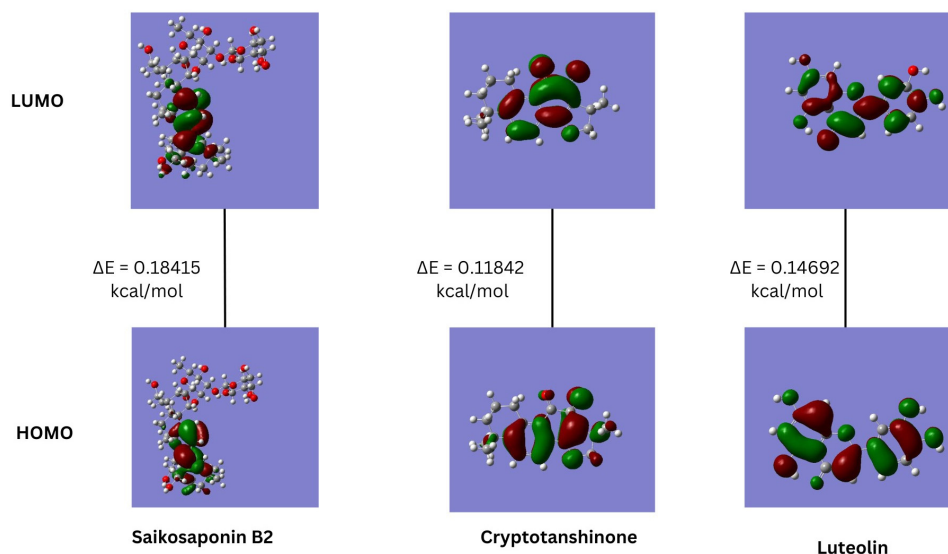


Figure 5. The band gap energies between HOMO and LUMO of saikosaponin B2, cryptotanshinone, and luteolin.

3.3. MD Simulations Analysis

Utilizing MD simulations, the stability and dynamic behavior of both apoprotein and protein–ligand complexes were investigated. Two terpenes (cryptotanshinone and saikosaponin B2) complexed with S1-RBD having high binding affinity and significant interactions were selected for the MD simulations. The structural changes, dynamic behavior, and stability of terpenes and their derivatives within the S1-RBD target protein were analyzed in terms of the RMSD, RMSF, R_g , SASA, and number of hydrogen bonds.

3.3.1. Root Mean Square Deviation (RMSD)

RMSD analysis provided access to the dynamic behavior in addition to the conformational and structural alterations within the backbone of the apoprotein and protein–ligand complexes [55]. From the 100 ns simulation trajectory, the RMSD plots of the apoprotein and protein–ligand complexes are displayed in Figure 6. The RMSD plots showed that both the apoprotein and cryptotanshinone–protein complex gained stability after 40 ns, but a slight fluctuation was observed within the backbone of the apoprotein after 75 ns, whereas the luteolin–protein complex gained stability after 25 ns. On the other hand, the saikosaponin B2–protein complex did not show considerable stability with a 100 ns simulation trajectory. The simulation results reveal that the luteolin–protein and the cryptotanshinone–protein formed the most stable complex in contrast to the apoprotein. The average RMSD value of all the complexes along with the apoprotein is displayed in Table 3.

Table 3. Average values of the RMSD, RMSF, R_g , and SASA of the protein–ligand complexes.

Complex	Cryptotanshinone–Protein Complex	Saikosaponin B2–Protein Complex	Luteolin–Protein Complex	Apoprotein
Average RMSD (nm)	0.3474	0.5433	0.2882	0.4101
Average RMSF (nm)	0.1465	0.1708	0.0943	0.1734
Average R_g (nm)	1.6846	1.7492	1.8122	1.8101
Average SASA (nm ²)	95.1708	98.0475	105.0639	96.006

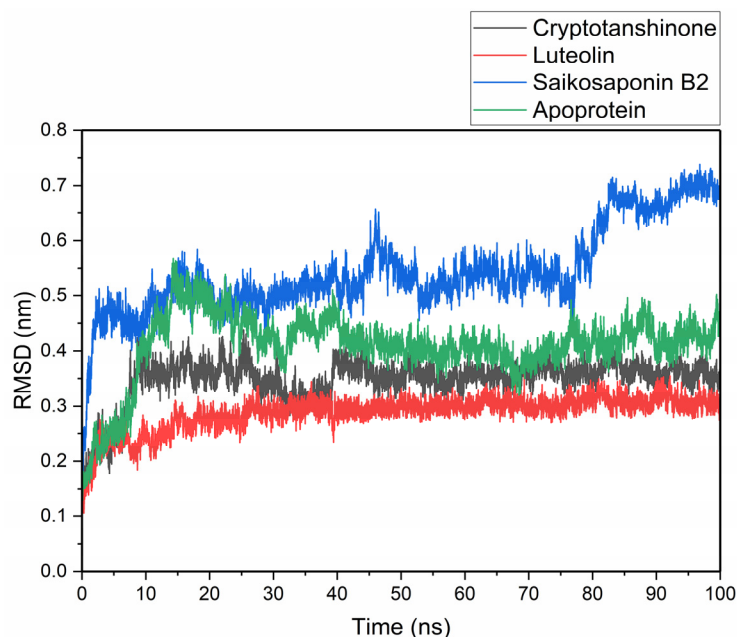


Figure 6. RMSD plots of the apoprotein and protein complexes of saikosaponin B2, cryptotanshinone, and luteolin.

3.3.2. Root Mean Square Fluctuations (RMSF)

The dynamic behavior occurring within the individual amino acids of the backbone of the apoprotein and the protein–ligand complexes was assessed via RMSF analysis. Higher RMSF values indicate more flexibility and mobility in particular protein regions, revealing information about the loop and protease-labile portions of the protein [56]. Similarly, the lower value of the RMSF indicates the secondary structure of proteins like helices and sheets. Both the complexes and apoprotein showed similar types of fluctuations in the same residues during the 100 ns simulation trajectory (Figure 7). The apoprotein, cryptotanshinone–protein, luteolin–protein, and saikosaponin B2–protein complexes have average RMSF values of 0.1734, 0.1465, 0.09434, and 0.1708 nm, respectively (Table 3). The apoprotein and all the ligand–protein complexes exhibited fluctuations in similar amino acid residues, which reveals that significant conformational changes do not occur in the protein after forming the complex with ligands. Similarly, the protein attains a secondary structure with helix and sheets after forming a complex with luteolin.

3.3.3. Radius of Gyration (R_g)

The R_g value was used to determine the stability and compactness of the apoprotein and protein–ligand complexes. Similarly, the R_g value is also crucial in determining the folded and unfolded nature of the apoprotein and protein–ligand complexes. The structural compactness of the apoprotein and protein–ligand complexes was estimated via MD simulation trajectory for evaluating the R_g value (Figure 8).

The apoprotein, cryptotanshinone–protein, saikosaponin B2–protein, and luteolin–protein complexes have average R_g values of 1.8101, 1.6846, 1.7492, and 1.8122 nm, respectively (Table 3). All the protein–ligand complexes along with the apoprotein exhibited comparatively stable and consistent R_g values. The R_g values indicate all complexes formed perfectly superimposed structures and had good stability. The R_g results reveal all three protein–ligand complexes along with the apoprotein achieved a folded conformation and compact structure during the 100 ns simulation trajectory. Similarly, cryptotanshinone and saikosaponin B2 have a lower R_g value compared to luteolin indicating cryptotanshinone and saikosaponin B2 form a more compact structure by binding effectively with key residues of the target protein.

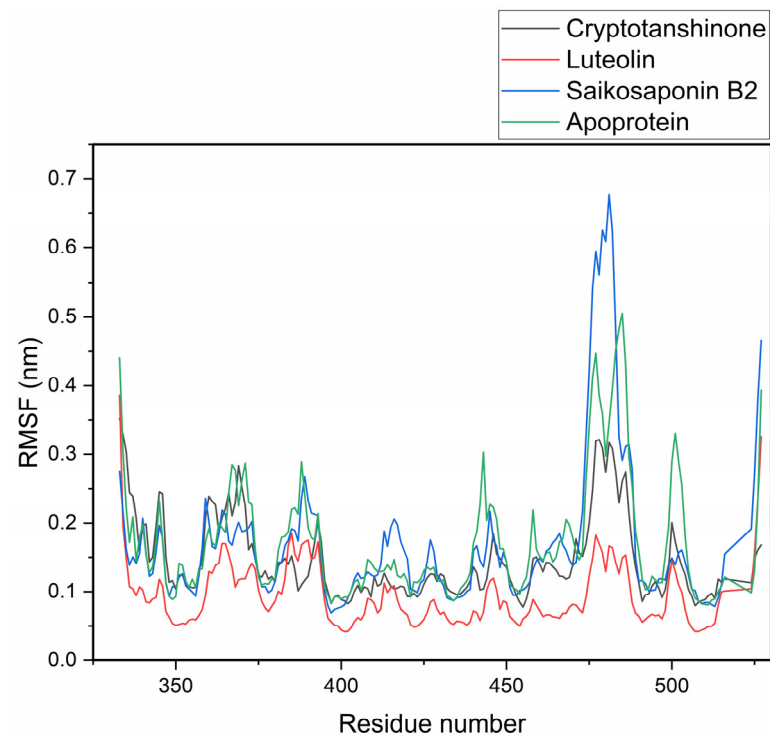


Figure 7. RMSF plots of the apoprotein and the protein complexes of saikosaponin B2, cryptotanshinone, and luteolin.

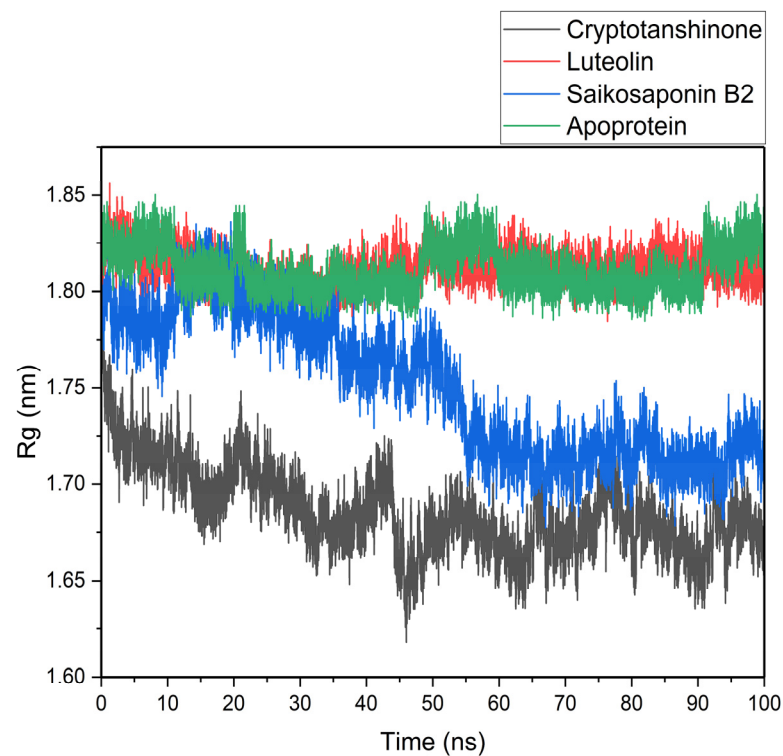


Figure 8. Rg plots of the apoprotein and protein complexes of saikosaponin B2, cryptotanshinone, and luteolin.

3.3.4. Solvent Accessible Surface Area (SASA)

The SASA parameter is used to assess the portion of the protein that is accessible to organic solvent and water. To evaluate the number of conformational changes that occur during interactions, the SASA parameter is crucial. The bound conformation of

biomolecules possesses a greater SASA value compared to the unbound one [57]. The lower value of SASA indicates that the formed complex has a compact structure, and less surface area is available for interaction with solvent molecules. The average SASA for the apoprotein, cryptotanshinone–protein, saikosaponin B2–protein, and luteolin–protein complexes were observed to be 96.006, 95.1708, 98.0475, and 105.0639 nm², respectively (Table 3). The SASA plot reveals that the cryptotanshinone binds effectively to the binding site of the protein and forms a more compact structure compared to saikosaponin B2 and luteolin. The SASA plot of all three complexes along with the apoprotein is displayed in Figure 9.

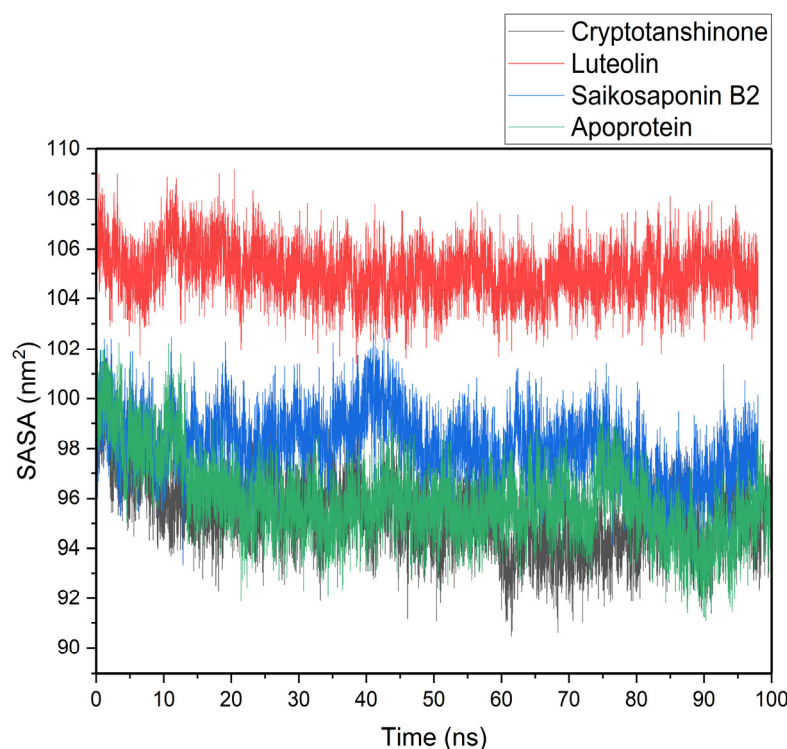


Figure 9. SASA plots of the apoprotein and protein complexes of saikosaponin B2, cryptotanshinone, and luteolin.

3.3.5. Hydrogen Bond Analysis

Because hydrogen bonds are essential for substrate binding to proteins and they affect many biological processes, including drug affinity, metabolism, adsorption, and specificity, it is necessary to identify hydrogen bond patterns by tracking the dynamic fluctuations in hydrogen bonds in all protein–ligand complexes. It was observed that the cryptotanshinone–protein, saikosaponin B2–protein, and luteolin–protein complexes maintained hydrogen bonding throughout the 100 ns simulation trajectory. The cryptotanshinone–protein complex exhibited up to three hydrogen bonds, whereas the saikosaponin B2–protein complex exhibited four hydrogen bonds, and the luteolin–protein complex exhibited up to five hydrogen bonds, as displayed in Figure 10.

3.4. Pharmacokinetic Analysis

To work effectively, a medicine should reach the target organ in an adequate amount and be in a biologically active state for sufficient time to permit the biochemical responses to occur [42]. Among a plethora of prediction models available, we relied on SwissADME, ProTox II, and the pkCSM Web server for exploration of the pharmacological effects of cryptotanshinone and luteolin. Octanol/water partition coefficients (logP values) characterize the lipophilicity of drugs, and according to Lipinski, a desirable lipophilicity range for compounds advancing to Phase II clinical trials is a logP < 5 [58,59]. Both cryptotanshinone and

luteolin demonstrated “drug-likeness” characteristics and followed Lipinski’s rule of five, which refers to the probability of a molecule acting as an oral drug. The topological polar surface area (TPSA) is a guideline to assess the capacity of a drug to permeate cells, and a TPSA $>140 \text{ \AA}^2$ denotes the poor permeability of drugs, while a TPSA $\leq 60 \text{ \AA}^2$ denotes high intestinal permeability [60,61]. Cryptotanshinone has a TPSA of less than 60 \AA^2 revealing high intestinal permeability, whereas luteolin has 111.13 \AA^2 TPSA revealing its moderate intestinal permeability. The drug-likeness of cryptotanshinone and luteolin is displayed in Table S3.

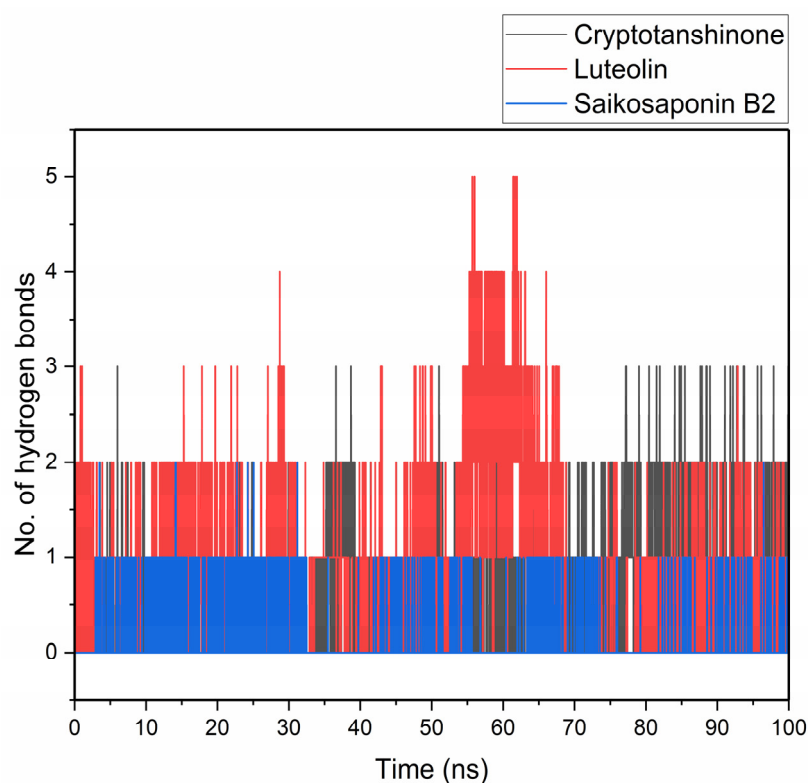


Figure 10. H-bonding plots of the protein complexes of saikosaponin B2, cryptotanshinone, and luteolin.

Additionally, the pkCSM webserver aids in evaluating a compound’s potency, pharmacological characteristics, and related safety concerns [43]. The primary location for oral drug absorption is the intestine, and an intestinal drug absorption of less than 30% is considered inadequate. Cryptotanshinone and luteolin have suitable intestinal absorption owing to their high intestinal absorption rates. Similarly, the water solubility of cryptotanshinone is appropriate to be a drug candidate. To evaluate the absorption and bioavailability of oral medications, the permeability of the colon cancer cell line (Caco-2) is assessed; an apparent permeability coefficient (Papp) value $> 8 \times 10^{-6} \text{ cm/s}$ is regarded as a good permeability value [62]. ADMET analysis (Table S4) revealed cryptotanshinone as moderately water soluble and with a low Caco-2 permeability, with no AMES toxicity and hepatotoxicity. To prevent neurotoxicity, it is preferable for drugs with an action site that is unrelated to the brain to not cross the blood–brain barrier (BBB) [63], and remarkably, cryptotanshinone and luteolin do not cross the BBB since compounds with a $\log_{BB} \leq 0.3$ are not adequately disseminated to the brain. Drug metabolism is shown by ADMET’s scanning of the CYP parameters [64]. The metabolism of cryptotanshinone in human liver microsomes may be attributed to the metabolic enzymes CYP1A2, CYP2A6, and CYP3A4 [65].

Moreover, for analyzing the toxicities, the ProTox-II server is helpful, according to which toxicity classes have been divided into six major groups: Class I and II (deadly if ingested), Class III (poisonous if ingested), Class IV (harmful if ingested), Class V (may be

harmful if ingested), and Class VI (non-toxic) [44]. Given that cryptotanshinone belongs to toxicity class VI, it might be a more effective medication than luteolin. Considering the MD simulation results, drug-likeness, and ADMET properties of cryptotanshinone, its S1-RBD assay was performed for further validation.

3.5. S1-RBD Binding Assay

An enzyme-linked immunosorbent assay was used to evaluate the *in vitro* activity of cryptotanshinone against the S1-RBD of the SARS-CoV-2 Omicron variant and hACE2. The *in vitro* results revealed that cryptotanshinone effectively inhibited the interaction of hACE2 with the S1-RBD protein with IC_{50} of $86.06 \pm 1.56 \mu\text{M}$ (Figure S3). Our data indicate that cryptotanshinone exhibits better inhibition compared to luteolin (having IC_{50} of 0.61 mM) [66], which further concludes that cryptotanshinone is an effective inhibitor of the interaction of hACE2 and S1-RBD.

Overall, our findings reveal that, in contrast to luteolin, which has previously demonstrated effectiveness through *in silico* [67] and *in vitro* analyses [66], cryptotanshinone exhibits superior inhibition against the spike S1-RBD protein.

4. Conclusions

The present study evaluated the inhibitory potential of 50 naturally existing terpenes against the spike protein of SARS-CoV-2, utilizing detailed *in silico* techniques followed by an *in vitro* study. In-depth computational analyses, encompassing favorable binding affinity and significant interactions with key residues, specifically Lys 440 and Trp 436, through molecular docking, coupled with robust reactivity within the binding pocket of the S1-RBD as determined by DFT analysis alongside stability of its complex analyzed through RMSD, RMSF, Rg, SASA, and H-bond parameters of MD simulation underline cryptotanshinone's potential as a potent drug candidate against the spike protein. Additionally, the promising pharmacokinetic properties further support cryptotanshinone's candidacy. The experimentally determined IC_{50} of $86.06 \pm 1.56 \mu\text{M}$ validates the inhibitory potential of cryptotanshinone against the S1-RBD of the SARS-CoV-2 Omicron variant. These findings underscore the importance of further research to comprehensively explore cryptotanshinone against SARS-CoV-2.

Supplementary Materials: The following supporting information can be downloaded at: <https://www.mdpi.com/article/10.3390/pr12010230/s1>, Table S1: Terpenes with antiviral activities; Table S2: PubChem ID and binding affinity of terpenes with S1-RBD of SARS CoV-2 Omicron variant; Table S3: Drug-like properties of cryptotanshinone and luteolin; Table S4: ADMET profiles of cryptotanshinone and luteolin; Figure S1: Structures of selected terpenes; Figure S2: Validation of docking protocol. (a) First docked luteolin (green) (b) second docked luteolin (magenta) and (c) superimposition of two docked luteolin (RMSD = 0.621 Å); Figure S3: Binding curve of hACE2 receptor to S1-RBD of SARS-CoV-2 in the presence of different concentrations of cryptotanshinone as determined by ELISA. (See Refs. [68–82]).

Author Contributions: Conceptualization, N.P., J.K.S. and B.P.R.; methodology, A.S., S.R.U. and B.K.R.; software, A.S., S.R.U. and B.K.R.; formal analysis, S.B.; writing—original draft preparation, A.S., S.R.U. and B.K.R.; writing—review and editing, N.P., J.K.S., B.P.R. and K.R.S.; supervision, N.P.; funding acquisition, A.S. All authors have read and agreed to the published version of the manuscript.

Funding: This research work is supported by the University Grants Commission, Nepal (Award No. PhD-78/79-S&T-06).

Data Availability Statement: Data are contained within the article and Supplementary Materials.

Acknowledgments: We would like to acknowledge Jhashanath (Subin) Adhikari for his computational lab support.

Conflicts of Interest: Author Salyan Bhattarai was employed by the company Paraza Pharma, Inc. The remaining authors declare that the research was conducted in the absence of any commercial or financial relationships that could be construed as a potential conflict of interest.

References

1. Christie, A.; Mbaeyi, S.A.; Walensky, R.P. CDC Interim Recommendations for Fully Vaccinated People: An Important First Step. *JAMA* **2021**, *325*, 1501. [[CrossRef](#)]
2. Liu, H.; Chen, J.; Shao, W.; Yan, S.; Ding, S. Efficacy and Safety of Novel Oral Antivirals in Hospitalized COVID-19 Patients: A Network Meta-Analysis of Randomized Clinical Trials. *Clin. Epidemiol.* **2023**, *15*, 1041–1053. [[CrossRef](#)]
3. Rana, R.; Kant, R.; Huirem, R.S.; Bohra, D.; Ganguly, N.K. Omicron Variant: Current Insights and Future Directions. *Microbiol. Res.* **2022**, *265*, 127204. [[CrossRef](#)]
4. Bazargan, M.; Elahi, R.; Esmaelizadeh, A.OMICRON: Virology, Immunopathogenesis, and Laboratory Diagnosis. *J. Gene Med.* **2022**, *24*, e3435. [[CrossRef](#)]
5. Gallagher, T.M.; Buchmeier, M.J. Coronavirus Spike Proteins in Viral Entry and Pathogenesis. *Virology* **2001**, *279*, 371–374. [[CrossRef](#)]
6. Zhao, Z.; Zhou, J.; Tian, M.; Huang, M.; Liu, S.; Xie, Y.; Han, P.; Bai, C.; Han, P.; Zheng, A.; et al. Omicron SARS-CoV-2 Mutations Stabilize Spike up-RBD Conformation and Lead to a Non-RBM-Binding Monoclonal Antibody Escape. *Nat. Commun.* **2022**, *13*, 4958. [[CrossRef](#)]
7. Mannar, D.; Saville, J.W.; Zhu, X.; Srivastava, S.S.; Berezuk, A.M.; Tuttle, K.S.; Marquez, A.C.; Sekirov, I.; Subramaniam, S. SARS-CoV-2 Omicron Variant: Antibody Evasion and Cryo-EM Structure of Spike Protein–ACE2 Complex. *Science* **2022**, *375*, 760–764. [[CrossRef](#)]
8. Cui, Z.; Liu, P.; Wang, N.; Wang, L.; Fan, K.; Zhu, Q.; Wang, K.; Chen, R.; Feng, R.; Jia, Z.; et al. Structural and Functional Characterizations of Infectivity and Immune Evasion of SARS-CoV-2 Omicron. *Cell* **2022**, *185*, 860–871.e13. [[CrossRef](#)]
9. Mani, J.S.; Johnson, J.B.; Steel, J.C.; Broszczak, D.A.; Neilsen, P.M.; Walsh, K.B.; Naiker, M. Natural Product-Derived Phytochemicals as Potential Agents against Coronaviruses: A Review. *Virus Res.* **2020**, *284*, 197989. [[CrossRef](#)]
10. Tahir ul Qamar, M.; Maryam, A.; Muneer, I.; Xing, F.; Ashfaq, U.A.; Khan, F.A.; Anwar, F.; Geesi, M.H.; Khalid, R.R.; Rauf, S.A.; et al. Computational Screening of Medicinal Plant Phytochemicals to Discover Potent Pan-Serotype Inhibitors against Dengue Virus. *Sci. Rep.* **2019**, *9*, 1433. [[CrossRef](#)]
11. Mumtaz, A.; Ashfaq, U.A.; ul Qamar, M.T.; Anwar, F.; Gulzar, F.; Ali, M.A.; Saari, N.; Pervez, M.T. MPD3: A Useful Medicinal Plants Database for Drug Designing. *Nat. Product. Res.* **2017**, *31*, 1228–1236. [[CrossRef](#)]
12. Bergman, M.E.; Davis, B.; Phillips, M.A. Medically Useful Plant Terpenoids: Biosynthesis, Occurrence, and Mechanism of Action. *Molecules* **2019**, *24*, 3961. [[CrossRef](#)]
13. Ricotta, E.; Kwan, J. Artemisinin-Resistant Malaria as a Global Catastrophic Biological Threat. In *Global Catastrophic Biological Risks*; Inglesby, T.V., Adalja, A.A., Eds.; Current Topics in Microbiology and Immunology; Springer: Cham, Switzerland, 2019; Volume 424, pp. 33–57; ISBN 978-3-030-36310-9.
14. Guimarães, A.C.; Meireles, L.M.; Lemos, M.F.; Guimarães, M.C.C.; Endringer, D.C.; Fronza, M.; Scherer, R. Antibacterial Activity of Terpenes and Terpenoids Present in Essential Oils. *Molecules* **2019**, *24*, 2471. [[CrossRef](#)]
15. Galle, M.; Crespo, R.; Rodenak Kladniew, B.; Montero Villegas, S.; Polo, M.; De Bravo, M.G. Suppression by Geraniol of the Growth of A549 Human Lung Adenocarcinoma Cells and Inhibition of the Mevalonate Pathway in Culture and In Vivo: Potential Use in Cancer Chemotherapy. *Nutr. Cancer* **2014**, *66*, 888–895. [[CrossRef](#)]
16. Zhu, L.; Chen, L. Progress in Research on Paclitaxel and Tumor Immunotherapy. *Cell Mol. Biol. Lett.* **2019**, *24*, 40. [[CrossRef](#)]
17. Turner, S.E.; Williams, C.M.; Iversen, L.; Whalley, B.J. Molecular Pharmacology of Phytocannabinoids. In *Phytocannabinoids*; Kinghorn, A.D., Falk, H., Gibbons, S., Kobayashi, J., Eds.; Progress in the Chemistry of Organic Natural Products; Springer: Cham, Switzerland, 2017; Volume 103, pp. 61–101; ISBN 978-3-319-45539-6.
18. Hassan, S.T.S.; Masarčíková, R.; Berchová, K. Bioactive Natural Products with Anti-Herpes Simplex Virus Properties. *J. Pharm. Pharmacol.* **2015**, *67*, 1325–1336. [[CrossRef](#)]
19. Bi, X.; Han, L.; Qu, T.; Mu, Y.; Guan, P.; Qu, X.; Wang, Z.; Huang, X. Anti-Inflammatory Effects, SAR, and Action Mechanism of Monoterpenoids from Radix Paeoniae Alba on LPS-Stimulated RAW 264.7 Cells. *Molecules* **2017**, *22*, 715. [[CrossRef](#)]
20. Gonzalez-Burgos, E.; Gomez-Serranillos, M.P. Terpene Compounds in Nature: A Review of Their Potential Antioxidant Activity. *Curr. Med. Chem.* **2012**, *19*, 5319–5341. [[CrossRef](#)]
21. Fu, J.; Huang, H.; Liu, J.; Pi, R.; Chen, J.; Liu, P. Tanshinone IIA Protects Cardiac Myocytes against Oxidative Stress-Triggered Damage and Apoptosis. *Eur. J. Pharmacol.* **2007**, *568*, 213–221. [[CrossRef](#)]
22. Maione, F.; Cantone, V.; Chini, M.G.; De Feo, V.; Mascolo, N.; Bifulco, G. Molecular Mechanism of Tanshinone IIA and Cryptotanshinone in Platelet Anti-Aggregating Effects: An Integrated Study of Pharmacology and Computational Analysis. *Fitoterapia* **2015**, *100*, 174–178. [[CrossRef](#)]
23. Cinatl, J.; Morgenstern, B.; Bauer, G.; Chandra, P.; Rabenau, H.; Doerr, H. Glycyrrhizin, an Active Component of Licorice Roots, and Replication of SARS-Associated Coronavirus. *Lancet* **2003**, *361*, 2045–2046. [[CrossRef](#)]
24. Bicchì, C.; Rubiolo, P.; Ballero, M.; Sanna, C.; Matteodo, M.; Esposito, F.; Zinzula, L.; Tramontano, E. HIV-1-Inhibiting Activity of the Essential Oil of *Ridolfia Segetum* and *Oenanthe Crocata*. *Planta Med.* **2009**, *75*, 1331–1335. [[CrossRef](#)]
25. Muhseen, Z.T.; Hameed, A.R.; Al-Hasani, H.M.H.; Tahir ul Qamar, M.; Li, G. Promising Terpenes as SARS-CoV-2 Spike Receptor-Binding Domain (RBD) Attachment Inhibitors to the Human ACE2 Receptor: Integrated Computational Approach. *J. Mol. Liq.* **2020**, *320*, 114493. [[CrossRef](#)]

26. Kumar, A.; Choudhir, G.; Shukla, S.K.; Sharma, M.; Tyagi, P.; Bhushan, A.; Rathore, M. Identification of Phytochemical Inhibitors against Main Protease of COVID-19 Using Molecular Modeling Approaches. *J. Biomol. Struct. Dyn.* **2021**, *39*, 3760–3770. [[CrossRef](#)]
27. Kim, S. Exploring Chemical Information in PubChem. *Curr. Protoc.* **2021**, *1*, e217. [[CrossRef](#)]
28. Pence, H.E.; Williams, A. ChemSpider: An Online Chemical Information Resource. *J. Chem. Educ.* **2010**, *87*, 1123–1124. [[CrossRef](#)]
29. Yuan, S.; Chan, H.C.S.; Hu, Z. Using PYMOL as a Platform for Computational Drug Design. *WIREs Comput. Mol. Sci.* **2017**, *7*, e1298. [[CrossRef](#)]
30. Verma, S.; Patil, V.M.; Gupta, M.K. Mutation Informatics: SARS-CoV-2 Receptor-Binding Domain of the Spike Protein. *Drug Discov. Today* **2022**, *27*, 103312. [[CrossRef](#)]
31. Morris, G.M.; Goodsell, D.S.; Halliday, R.S.; Huey, R.; Hart, W.E.; Belew, R.K.; Olson, A.J. Automated Docking Using a Lamarckian Genetic Algorithm and an Empirical Binding Free Energy Function. *J. Comput. Chem.* **1998**, *19*, 1639–1662. [[CrossRef](#)]
32. Lan, J.; Ge, J.; Yu, J.; Shan, S.; Zhou, H.; Fan, S.; Zhang, Q.; Shi, X.; Wang, Q.; Zhang, L.; et al. Structure of the SARS-CoV-2 Spike Receptor-Binding Domain Bound to the ACE2 Receptor. *Nature* **2020**, *581*, 215–220. [[CrossRef](#)]
33. Jawad, B.; Adhikari, P.; Podgornik, R.; Ching, W.-Y. Key Interacting Residues between RBD of SARS-CoV-2 and ACE2 Receptor: Combination of Molecular Dynamics Simulation and Density Functional Calculation. *J. Chem. Inf. Model.* **2021**, *61*, 4425–4441. [[CrossRef](#)]
34. Elekofehinti, O.O.; Ejelolu, O.C.; Kamdem, J.P.; Akinlosotu, O.B.; Famuti, A.; Adebowale, D.D.; Iwaloye, O.; Bulu, Y.I.; Kade, I.J.; Rocha, J.B.T. Discovery of Potential Visfatin Activators Using in Silico Docking and ADME Predictions as Therapy for Type 2 Diabetes. *Beni-Suef Univ. J. Basic. Appl. Sci.* **2018**, *7*, 241–249. [[CrossRef](#)]
35. Saliu, T.P.; Umar, H.I.; Ogunbile, O.J.; Okpara, M.O.; Yanaka, N.; Elekofehinti, O.O. Molecular Docking and Pharmacokinetic Studies of Phytocompounds from Nigerian Medicinal Plants as Promising Inhibitory Agents against SARS-CoV-2 Methyltransferase (Nsp16). *J. Genet. Eng. Biotechnol.* **2021**, *19*, 172. [[CrossRef](#)]
36. Gill, P.M.W.; Johnson, B.G.; Pople, J.A.; Frisch, M.J. The Performance of the Becke–Lee–Yang–Parr (B–LYP) Density Functional Theory with Various Basis Sets. *Chem. Phys. Lett.* **1992**, *197*, 499–505. [[CrossRef](#)]
37. Vektariene, A.; Vektaris, G.; Svoboda, J. A Theoretical Approach to the Nucleophilic Behavior of Benzofused Thieno[3,2-b]Furans Using DFT and HF Based Reactivity Descriptors. *Arkivoc* **2009**, *2009*, 311–329. [[CrossRef](#)]
38. Anigboro, A.A.; Avwioroko, O.J.; Akeghware, O.; Tonukari, N.J. Anti-Obesity, Antioxidant and in Silico Evaluation of Justicia Carne Bioactive Compounds as Potential Inhibitors of an Enzyme Linked with Obesity: Insights from Kinetics, Semi-Empirical Quantum Mechanics and Molecular Docking Analysis. *Biophys. Chem.* **2021**, *274*, 106607. [[CrossRef](#)]
39. Cao, Z.; Liu, L.; Wang, J. Why the OPLS-AA Force Field Cannot Produce the β -Hairpin Structure of H1 Peptide in Solution When Comparing with the GROMOS 43A1 Force Field? *J. Biomol. Struct. Dyn.* **2011**, *29*, 527–539. [[CrossRef](#)]
40. Schüttelkopf, A.W.; van Aalten, D.M.F. PRODRG: A Tool for High-Throughput Crystallography of Protein–Ligand Complexes. *Acta Crystallogr. D Biol. Crystallogr.* **2004**, *60*, 1355–1363. [[CrossRef](#)]
41. Berendsen, H.J.C.; Postma, J.P.M.; van Gunsteren, W.F.; Hermans, J. Interaction Models for Water in Relation to Protein Hydration. In *Intermolecular Forces*; Pullman, B., Ed.; The Jerusalem Symposia on Quantum Chemistry and Biochemistry; Springer: Dordrecht, The Netherlands, 1981; Volume 14, pp. 331–342; ISBN 978-90-481-8368-5.
42. Daina, A.; Michielin, O.; Zoete, V. SwissADME: A Free Web Tool to Evaluate Pharmacokinetics, Drug-Likeness and Medicinal Chemistry Friendliness of Small Molecules. *Sci. Rep.* **2017**, *7*, 42717. [[CrossRef](#)]
43. Pires, D.E.V.; Blundell, T.L.; Ascher, D.B. pkCSM: Predicting Small-Molecule Pharmacokinetic and Toxicity Properties Using Graph-Based Signatures. *J. Med. Chem.* **2015**, *58*, 4066–4072. [[CrossRef](#)]
44. Banerjee, P.; Eckert, A.O.; Schrey, A.K.; Preissner, R. ProTox-II: A Webserver for the Prediction of Toxicity of Chemicals. *Nucleic Acids Res.* **2018**, *46*, W257–W263. [[CrossRef](#)]
45. Gangadevi, S.; Badavath, V.N.; Thakur, A.; Yin, N.; De Jonghe, S.; Acevedo, O.; Jochmans, D.; Leyssen, P.; Wang, K.; Neyts, J.; et al. Kobophenol A Inhibits Binding of Host ACE2 Receptor with Spike RBD Domain of SARS-CoV-2, a Lead Compound for Blocking COVID-19. *J. Phys. Chem. Lett.* **2021**, *12*, 1793–1802. [[CrossRef](#)]
46. Umar, H.I.; Josiah, S.S.; Saliu, T.P.; Jimoh, T.O.; Ajayi, A.; Danjuma, J.B. In-Silico Analysis of the Inhibition of the SARS-CoV-2 Main Protease by Some Active Compounds from Selected African Plants. *J. Taibah Univ. Med. Sci.* **2021**, *16*, 162–176. [[CrossRef](#)]
47. Da Costa, C.H.S.; De Freitas, C.A.B.; Alves, C.N.; Lameira, J. Assessment of Mutations on RBD in the Spike Protein of SARS-CoV-2 Alpha, Delta and Omicron Variants. *Sci. Rep.* **2022**, *12*, 8540. [[CrossRef](#)]
48. Ong, Q.; Ronnie Teo, J.W.; Dela Cruz, J.; Wee, E.; Wee, W.; Han, W. Irradiation of UVC LED at 277 Nm Inactivates Coronaviruses in Association to Photodegradation of Spike Protein. *Heliyon* **2022**, *8*, e11132. [[CrossRef](#)]
49. Guo, Y.; Han, J.; Zhang, Y.; He, J.; Yu, W.; Zhang, X.; Wu, J.; Zhang, S.; Kong, Y.; Guo, Y.; et al. SARS-CoV-2 Omicron Variant: Epidemiological Features, Biological Characteristics, and Clinical Significance. *Front. Immunol.* **2022**, *13*, 877101. [[CrossRef](#)]
50. SM Abd El-Kareem, M.; ARabbih, M.; Elansary, H.O.; AAl-Mana, F. Mass Spectral Fragmentation of Pelargonium Graveolens Essential Oil Using GC–MS Semi-Empirical Calculations and Biological Potential. *Processes* **2020**, *8*, 128. [[CrossRef](#)]
51. Huang, Y.; Rong, C.; Zhang, R.; Liu, S. Evaluating Frontier Orbital Energy and HOMO/LUMO Gap with Descriptors from Density Functional Reactivity Theory. *J. Mol. Model.* **2017**, *23*, 3. [[CrossRef](#)]
52. Kumar, C.B.P.; Raghu, M.S.; Prasad, K.N.N.; Chandrasekhar, S.; Jayanna, B.K.; Alharthi, F.A.; Prashanth, M.K.; Kumar, K.Y. Investigation of Biological Activity of 2,3-Disubstituted Quinazolin-4(1H)-Ones against *Mycobacterium tuberculosis* and DNA via Docking, Spectroscopy and DFT Studies. *New J. Chem.* **2021**, *45*, 403–414. [[CrossRef](#)]

53. Xu, H.; Tu, X.; Fan, G.; Wang, Q.; Wang, X.; Chu, X. Adsorption Properties Study of Boron Nitride Fullerene for the Application as Smart Drug Delivery Agent of Anti-Cancer Drug Hydroxyurea by Density Functional Theory. *J. Mol. Liq.* **2020**, *318*, 114315. [CrossRef]
54. De Proft, F.; Geerlings, P. Conceptual and Computational DFT in the Study of Aromaticity. *Chem. Rev.* **2001**, *101*, 1451–1464. [CrossRef]
55. Muralidharan, N.; Sakthivel, R.; Velmurugan, D.; Gromiha, M.M. Computational Studies of Drug Repurposing and Synergism of Lopinavir, Oseltamivir and Ritonavir Binding with SARS-CoV-2 Protease against COVID-19. *J. Biomol. Struct. Dyn.* **2021**, *39*, 2673–2678. [CrossRef]
56. Ilyas, U.; Nazir, B.; Altaf, R.; Muhammad, S.A.; Zafar, H.; Paiva-Santos, A.C.; Abbas, M.; Duan, Y. Investigation of Anti-Diabetic Potential and Molecular Simulation Studies of Dihydropyrimidinone Derivatives. *Front. Endocrinol.* **2022**, *13*, 1022623. [CrossRef]
57. Chakravarty, D.; Guharoy, M.; Robert, C.H.; Chakrabarti, P.; Janin, J. Reassessing Buried Surface Areas in Protein–Protein Complexes. *Protein Sci.* **2013**, *22*, 1453–1457. [CrossRef]
58. Waring, M.J. Lipophilicity in Drug Discovery. *Expert. Opin. Drug Discov.* **2010**, *5*, 235–248. [CrossRef]
59. Lipinski, C.A.; Lombardo, F.; Dominy, B.W.; Feeney, P.J. Experimental and Computational Approaches to Estimate Solubility and Permeability in Drug Discovery and Development Settings 1PII of Original Article: S0169-409X(96)00423-1. *Adv. Drug Deliv. Rev.* **1997**, *23*, 3–25, Erratum in *Adv. Drug Deliv. Rev.* **2001**, *46*, 3–26. [CrossRef]
60. Fernandes, J.; Gattass, C.R. Topological Polar Surface Area Defines Substrate Transport by Multidrug Resistance Associated Protein 1 (MRP1/ABCC1). *J. Med. Chem.* **2009**, *52*, 1214–1218. [CrossRef]
61. Van de Waterbeemd, H. In Silico Models to Predict Oral Absorption. In *Comprehensive Medicinal Chemistry II*; Elsevier: Amsterdam, The Netherlands, 2007; pp. 669–697. ISBN 978-0-08-045044-5.
62. Lagorce, D.; Douguet, D.; Miteva, M.A.; Villoutreix, B.O. Computational Analysis of Calculated Physicochemical and ADMET Properties of Protein-Protein Interaction Inhibitors. *Sci. Rep.* **2017**, *7*, 46277. [CrossRef]
63. Muehlbacher, M.; Spitzer, G.M.; Liedl, K.R.; Kornhuber, J. Qualitative Prediction of Blood–Brain Barrier Permeability on a Large and Refined Dataset. *J. Comput. Aided Mol. Des.* **2011**, *25*, 1095–1106. [CrossRef]
64. Wu, X.; Wang, J.; Tan, L.; Bui, J.; Gjerstad, E.; McMillan, K.; Zhang, W. In Vitro ADME Profiling Using High-Throughput RapidFire Mass Spectrometry: Cytochrome P450 Inhibition and Metabolic Stability Assays. *SLAS Discov.* **2012**, *17*, 761–772. [CrossRef]
65. Zeng, J.; Fan, Y.; Tan, B.; Su, H.; Li, Y.; Zhang, L.; Jiang, J.; Qiu, F. Characterizing the Metabolism of Cryptotanshinone by Human P450 Enzymes and Uridine Diphosphate Glucuronosyltransferases in Vitro. *Acta Pharmacol. Sin.* **2018**, *39*, 1393–1404. [CrossRef]
66. Zhu, J.; Yan, H.; Shi, M.; Zhang, M.; Lu, J.; Wang, J.; Chen, L.; Wang, Y.; Li, L.; Miao, L.; et al. Luteolin Inhibits Spike Protein of Severe Acute Respiratory Syndrome Coronavirus-2 (SARS-CoV-2) Binding to Angiotensin-converting Enzyme 2. *Phytother. Res.* **2023**, *37*, 3508–3521. [CrossRef]
67. Ansari, W.A.; Ahamad, T.; Khan, M.A.; Khan, Z.A.; Khan, M.F. Exploration of Luteolin as Potential Anti-COVID-19 Agent: Molecular Docking, Molecular Dynamic Simulation, ADMET and DFT Analysis. *Lett. Drug Design Discov.* **2022**, *19*, 741–756. [CrossRef]
68. Sawadjoon, S.; Kittakoop, P.; Isaka, M.; Kirtikara, K.; Madla, S.; Thebtaranonth, Y. Antiviral and Antiplasmodial Spirodihydrobenzofuran Terpenes from the Fungus *Stachybotrys nephrospora*. *Planta Med.* **2004**, *70*, 1085–1087. [CrossRef]
69. Yoshimoto, J.; Kakui, M.; Iwasaki, H.; Fujiwara, T.; Sugimoto, H.; Hattori, N. Identification of a Novel HA Conformational Change Inhibitor of Human Influenza Virus. *Arch. Virol.* **1999**, *144*, 865–878. [CrossRef]
70. Phytochemical Analysis and in Vitro Antiviral Activities of the Essential Oils of Seven Lebanon Species—Loizzo—2008—Chemistry & Biodiversity—Wiley Online Library. Available online: <https://onlinelibrary.wiley.com/doi/10.1002/cbdv.200890045> (accessed on 15 January 2024).
71. Nagoor Meeran, M.F.; Seenipandi, A.; Javed, H.; Sharma, C.; Hashiesh, H.M.; Goyal, S.N.; Jha, N.K.; Ojha, S. Can Limonene Be a Possible Candidate for Evaluation as an Agent or Adjuvant against Infection, Immunity, and Inflammation in COVID-19? *Heliyon* **2021**, *7*, e05703. [CrossRef]
72. Wen, C.-C.; Kuo, Y.-H.; Jan, J.-T.; Liang, P.-H.; Wang, S.-Y.; Liu, H.-G.; Lee, C.-K.; Chang, S.-T.; Kuo, C.-J.; Lee, S.-S.; et al. Specific Plant Terpenoids and Lignoids Possess Potent Antiviral Activities against Severe Acute Respiratory Syndrome Coronavirus. *J. Med. Chem.* **2007**, *50*, 4087–4095. [CrossRef]
73. Zhang, G.-J.; Li, Y.-H.; Jiang, J.-D.; Yu, S.-S.; Wang, X.-J.; Zhuang, P.-Y.; Zhang, Y.; Qu, J.; Ma, S.-G.; Li, Y.; et al. Diterpenes and Sesquiterpenes with Anti-Coxsackie Virus B3 Activity from the Stems of *Illicium Jiadifengpi*. *Tetrahedron* **2014**, *70*, 4494–4499. [CrossRef]
74. Wang, Y.-D.; Zhang, G.-J.; Qu, J.; Li, Y.-H.; Jiang, J.-D.; Liu, Y.-B.; Ma, S.-G.; Li, Y.; Lv, H.-N.; Yu, S.-S. Diterpenoids and Sesquiterpenoids from the Roots of *Illicium Majus*. *J. Nat. Prod.* **2013**, *76*, 1976–1983. [CrossRef]
75. Park, J.-Y.; Kim, J.H.; Kim, Y.M.; Jeong, H.J.; Kim, D.W.; Park, K.H.; Kwon, H.-J.; Park, S.-J.; Lee, W.S.; Ryu, Y.B. Tanshinones as Selective and Slow-Binding Inhibitors for SARS-CoV Cysteine Proteases. *Bioorganic Med. Chem.* **2012**, *20*, 5928–5935. [CrossRef]
76. Astani, A.; Reichling, J.; Schnitzler, P. Comparative Study on the Antiviral Activity of Selected Monoterpenes Derived from Essential Oils. *Phytother. Res.* **2010**, *24*, 673–679. [CrossRef] [PubMed]
77. Cheng, P.-W.; Ng, L.-T.; Chiang, L.-C.; Lin, C.-C. Antiviral Effects of Saikosaponins on Human Coronavirus 229e in Vitro. *Clin. Exp. Pharmacol. Physiol.* **2006**, *33*, 612–616. [CrossRef]

78. Ryu, Y.B.; Park, S.-J.; Kim, Y.M.; Lee, J.-Y.; Seo, W.D.; Chang, J.S.; Park, K.H.; Rho, M.-C.; Lee, W.S. SARS-CoV 3CLpro Inhibitory Effects of Quinone-Methide Triterpenes from *Tripterygium Regelii*. *Bioorganic Med. Chem. Lett.* **2010**, *20*, 1873–1876. [[CrossRef](#)]
79. Viruses | Free Full-Text | Anti-Infectivity against Herpes Simplex Virus and Selected Microbes and Anti-Inflammatory Activities of Compounds Isolated from *Eucalyptus Globulus* Labill. Available online: <https://www.mdpi.com/1999-4915/10/7/360> (accessed on 15 January 2024).
80. Evaluation of in Vitro Antiviral Activity of Essential Oil Compounds Against Dengue Virus | Pharmacognosy Journal. Available online: <https://phcogj.com/article/470> (accessed on 15 January 2024).
81. Hoever, G.; Baltina, L.; Michaelis, M.; Kondratenko, R.; Baltina, L.; Tolstikov, G.A.; Doerr, H.W.; Cinatl, J. Antiviral Activity of Glycyrrhizic Acid Derivatives against SARS–Coronavirus. *J. Med. Chem.* **2005**, *48*, 1256–1259. [[CrossRef](#)]
82. Niedermeyer, T.H.J.; Lindequist, U.; Mentel, R.; Gördes, D.; Schmidt, E.; Thurow, K.; Lalk, M. Antiviral Terpenoid Constituents of *Ganoderma Pfeifferi*. *J. Nat. Prod.* **2005**, *68*, 1728–1731. [[CrossRef](#)]

Disclaimer/Publisher’s Note: The statements, opinions and data contained in all publications are solely those of the individual author(s) and contributor(s) and not of MDPI and/or the editor(s). MDPI and/or the editor(s) disclaim responsibility for any injury to people or property resulting from any ideas, methods, instructions or products referred to in the content.